# Measurement of cosmic-ray low-energy antiproton spectrum with the first BESS-Polar Antarctic flight

K. Abe [a,1], H. Fuke [b], S. Haino [c,2,*], T. Hams [d,3], A. Itazaki [a], K. C. Kim [e], T. Kumazawa [c], M. H. Lee [e], Y. Makida [c], S. Matsuda [c], K. Matsumoto [c], J. W. Mitchell [d], A. A. Moiseev [d], Z. Myers [e,4], J. Nishimura [f], M. Nozaki [c], R. Orito [a,5], J. F. Ormes [g], M. Sasaki [d], E. S. Seo [e], Y. Shikaze [a,6], R. E. Streitmatter [d], J. Suzuki [c], Y. Takasugi [a], K. Takeuchi [a], K. Tanaka [c], T. Yamagami [b], A. Yamamoto [c], T. Yoshida [b], K. Yoshimura [c]

[a] *Kobe University, Kobe, Hyogo 657-8501, Japan*

[b] *Institute of Space and Astronautical Science, Japan Aerospace Exploration Agency (ISAS/JAXA), Sagamihara, Kanagawa 229-8510, Japan*

[c] *High Energy Accelerator Research Organization (KEK), Tsukuba, Ibaraki 305-0801, Japan*

[d] *National Aeronautics and Space Administration, Goddard Space Flight Center (NASA/GSFC), Greenbelt, MD 20771, USA*

[e] *IPST, University of Maryland, College Park, MD 20742, USA*

[f] *The University of Tokyo, Bunkyo, Tokyo 113-0033 Japan*

[g] *Denver University, Denver, CO 80208, USA*

**Abstract**

The BESS-Polar spectrometer had its first successful balloon flight over Antarctica in December 2004. During the 8.5-day long-duration flight, almost 0.9 billion events were recorded and 1,520 antiprotons were detected in the energy range 0.1–4.2 GeV. In this paper, we report the antiproton spectrum obtained, discuss the origin of cosmic-ray antiprotons, and use antiprotons to probe the effect of charge sign dependent drift in the solar modulation.

*Key words:* cosmic-ray antiproton, solar modulation, superconducting spectrometer
*PACS:* 95.85.Ry, 96.40.Kk, 98.70.Sa

## 1 Introduction

Antiproton spectra have been measured by BESS (Balloon-borne Experiment with a Superconducting Spectrometer) in a series of flights from Lynn Lake, Canada providing reasonable statistics above 1 GeV [1,2,3,4,5,6,7]. Below 1 GeV statistics are limited and the effects of solar modulation are greater. The spectrum has a distinct peak around 2 GeV, showing the characteristic feature of secondary antiprotons produced by the interaction of Galactic cosmic-rays with the interstellar medium. The energy spectrum of these secondary antiprotons should decrease rapidly toward lower energies reflecting the kinematic constraints on antiproton production [8,9,10] and toward higher energies reflecting the steep power-law spectra of primary particles producing the antiprotons. In addition to these secondary antiprotons, there might be a source of primary antiprotons. Such sources have been suggested to result from the evaporation of primordial black holes (PBH) or from the annihilation of neutralino dark matter [11,12,13,14]. The spectrum of antiprotons from a primary source might have a peak in the energy region below 1 GeV, giving a flatter composite spectrum with excess flux compared to the purely secondary spectrum [10,13]. The influence of a low energy primary peak would be most evident at solar minimum [12,13] and BESS (1995+1997) measurements during this period [3,4] suggested this possibility. On the other hand, BESS-1998 [5] and subsequent measurements [6,7], which were taken after the solar minimum period, are more consistent with pure secondary nature. In order to resolve the important questions regarding possible novel sources, we undertook the higher precision measurements reported here.

In addition, we can use the charge sign difference of antiprotons to explore effects of drift in the solar modulation. A detailed understanding of the effects of solar modulation is important to establish the existence of any primary sources. During the positive polarity phase of solar activity before 2000 the measured antiproton-to-proton ($\bar{\mathrm{p}}/\mathrm{p}$) ratio [5] showed no distinctive variation. After the reversal of the solar magnetic field in 2000, a sudden increase of

* Corresponding author.
*Email address:* haino@post.kek.jp (S. Haino).
[1] Present address: Kamioka Observatory, ICRR, The University of Tokyo, Kamioka, Gifu 506-1205, Japan
[2] Present address: Istituto Nazionale di Fisica Nucleare (INFN), Perugia 06123, Italy
[3] Also at: CRESST/USRA, Columbia, MD 21044, USA
[4] Present address: Physics Department, Technion - Israel Institute of Technology, Technion City, Haifa 32000, Israel.
[5] Present address: Max-Planck-Institut für Physik, München 80805, Germany
[6] Present address: Japan Atomic Energy Agency (JAEA), Tokai-mura, Naka-gun, Ibaraki 319-1195, Japan

the $\bar{p}/p$ ratio [6] was clearly observed. Our measurements, as well as measurements of positron fraction ($e^+/(e^+ + e^-)$) [15], generally support recent calculations [10,16] incorporating steady-state drift models and charge-dependent effects of solar modulation. Protons and antiprotons have significantly different interstellar spectra and the drift directions are opposite because of the opposite charge sign. The combination of these effects implies that the $\bar{p}/p$ ratio should display a more interesting evolution [16] during 2000-2010 than it did during the 1990's. The secondary antiprotons are also useful to probe the average cosmic-ray proton spectrum over a large region of the Galaxy [17].

The BESS-Polar experiment was proposed as an advanced BESS program of long-duration balloon flights over Antarctica and has been prepared since 2001 [18,19,20] to further investigate elementary particle phenomena in the early Universe through a precise measurement of the low-energy antiproton spectrum and to search for primary antinuclei in cosmic rays. We report here a measurement of the cosmic-ray antiproton spectrum based on 1,520 antiproton events detected during an 8.5-day flight of the BESS-Polar spectrometer performed in December 2004. We discuss the origin of cosmic-ray antiprotons, and the solar modulation effect based on the measured $\bar{p}/p$ ratio.

## 2 Spectrometer

The BESS-Polar superconducting spectrometer, shown in Fig. 1, has been developed to reduce material thickness along the particle trajectory and to meet severe requirements for long duration balloon flights over Antarctica [18,20]. The basic instrument concepts, such as the cylindrical configuration with an open and wide acceptance and redundant measurements for particle identification, are inherited from the BESS spectrometer [21]. A very low instrumental energy cutoff for antiprotons was achieved with a new thin-walled ($2.46 g/cm^2$/wall including cryostat) superconducting magnet [22,23] using a new high-strength aluminum-stabilized superconductor. In addition, the outer pressure vessel was eliminated and the detectors were reconfigured. Low-energy particles only have to traverse 4.5 $g/cm^2$ of instrument material to be detected, about one quarter of that in the previous BESS spectrometer [21,24]. With these changes, the lowest energy for antiproton detection has been reduced to 0.1 GeV at the top of atmosphere (TOA).

A uniform field of 0.8 Tesla is produced by the superconducting coil, and its continuous operation is maintained for over 11 days with a 400-liter liquid helium reservoir. A JET-cell type drift chamber (JET) and two inner drift chambers (IDCs), which were also used in the BESS-TeV spectrometer [24,25], are placed inside the warm bore (0.80 m in diameter and 1.4 m in length). The JET and IDCs are filled and flowed with $CO_2$ gas using a semi-active flow

control system. Tracking of an incident particle in the $x-y$ plane (perpendicular to the magnetic field) inside the JET and IDCs is performed by fitting up to 52 hit-points, each with 150 $\mu$m resolution, resulting in a magnetic-rigidity (momentum divided by electric charge) resolution of 0.4 % at 1 GV, and a maximum detectable rigidity (MDR) of 240 GV. Tracking in the $z$ coordinate (parallel to the magnetic field direction) is done by fitting points inside IDCs measured by vernier pads with an accuracy of 1.0 mm and points in JET measured by charge division with an accuracy of 37 mm. The continuous and redundant 3-dimensional tracking enables BESS-Polar to distinguish backgrounds such as tracks having interactions or scatterings. A truncated mean of the integrated charges of the hit-pulses from the JET also provides an energy loss ($\mathrm{d}E/\mathrm{d}x$) measurement with a resolution of 10 %.

The top and bottom scintillator hodoscopes measure time-of-flight (TOF) and make two independent $\mathrm{d}E/\mathrm{d}x$ measurements. The scintillator hodoscopes consist of 10 top and 12 bottom plastic scintillators with a cross section of 96.5 mm (width) $\times$ 10 mm (thickness) and with photo-multiplier tubes (PMTs) attached by acrylic light guides at each end. The timing resolution of each hodoscope is 110 ps resulting in a $\beta^{-1}$ resolution of 3.3 %. In addition, a thin scintillator middle-TOF (MTOF) is installed on the lower surface of the solenoid bore to detect low energy particles which cannot penetrate the magnet wall. The MTOF consists of 64 plastic scintillator bars with a cross section of 10 mm (width) $\times$ 5 mm (thickness) read by multi-anode PMTs. The $\beta$ of the low energy antiprotons can be measured as a combination of top-middle TOF with a $\beta^{-1}$ resolution of 4.5 % below 0.6 GV (0.2 GeV for proton and antiproton). A Čerenkov counter with silica-aerogel radiator (ACC) is installed below the magnet. The radiator is selected to have a refractive index of 1.02 in order to veto $e^-/\mu^-$ backgrounds up to 4.2 GeV. The top and bottom TOF hodoscopes and the ACC operate at ambient pressure.

The event data acquisition sequence is initiated by a coincidence of signals in the top-bottom TOF or top-middle TOF hodoscopes [26]. Based on digitized detector information sent from the front end electronics, the event data are built and recorded to onboard hard disk drives with a total capacity of 3.5 Tera Bytes. During the Antarctic flight, the data acquisition rate was around 1.4 kHz, and the dead time was 150 $\mu$s (20 % of the data taking time). To supply electric power to the electronics onboard the payload, a solar cell array of 900 W capacity is mounted on an omni-directional octagonal frame around the payload. The total power consumption of the spectrometer was 420 W.

## 3 Data Analysis

### *3.1 Balloon flight observation*

The first BESS-Polar long duration balloon flight over Antarctica was launched from Williams Field (77°51.8′S, 167°5.4′E) near McMurdo Station on December 13, 2004 [27]. During the flight, some PMTs of the TOF hodoscopes had to be turned off because they were drawing excessive current, and the effective geometrical acceptance was consequently reduced to 70 % of the design value. The flight was terminated on December 21 and the payload landed at the south end of the Ross Ice Shelf (83°6.0′S, 155°35.4′W) after a continuous observation period of 8.5 days. The flight trajectory was close enough to the South magnetic pole that the geomagnetic cutoff rigidity was below 0.2 GV, lower than the lowest detection limit of the spectrometer. During the live data taking time of 507,075 seconds at an average floating altitude of 38.5 km (residual atmosphere of 4.3 g/cm$^2$), 894,482,590 cosmic-ray events were accumulated without any online event selection as 2.14 terabytes of data recorded on the hard disk drives.

### *3.2 Event selection*

Since the spectrometer is cylindrically symmetric, we can assume that antiprotons behave exactly like protons in the instrument except for the sign of their deflection in the magnetic field and their inelastic interactions. Thus, all the selection criteria were defined based on the measured properties of protons. At first, we selected events with (1) a single track and a downward-going particle fully contained in the fiducial region of the tracking volume, (2) only one or two hits each in the top and bottom TOF hodoscopes, (3) the hit position at the TOF hodoscopes consistent with the extrapolated track inside JET and IDCs, (4) cosine of zenith angle of the incident particle larger than 0.8, and (5) either top or bottom TOF hodoscopes read by PMTs at both ends. As a consequence of (5), the effective geometrical acceptance had to be further reduced to be 40 % of the design value.

The selection efficiency was estimated using a Monte Carlo (MC) simulation by applying the same selection criteria to the simulated events as to the observed data. The MC simulation was based on a GEANT3/GHEISHA code [28,29] and tuned to reproduce the results of an accelerator beam test of the previous BESS spectrometer [30] in which the detector configuration and materials are similar to the BESS-Polar spectrometer. The efficiency varied from 84.2±5.0 % at 0.2 GeV to 90.1±5.0 % at 2.0 GeV. The systematic error of the efficiency

was determined using the accelerator beam test data. Each analog-to-digital board for TOF has an individual dead time due to the period of switching reference capacitors used for baseline subtraction. Events digitized during the dead time have incorrect charge data and were rejected to ensure the quality of the data. The efficiency of surviving this cut was estimated as 77.8±0.1 % at 0.2 GeV and 78.8±0.1 % at 2.0 GeV. Here and in the selections described below, we used a sample of the proton data to determine the efficiencies.

The following track quality cuts were applied: (1) the reduced $\chi^2$ in the $x$–$y$ and $y$–$z$ track fitting to be less than 5, (2) the fitting error on the curvature (inverse rigidity) to be less than 0.015 $\mathrm{GV}^{-1}$, (3) the track fitting path length to be longer than 500 mm, and (4) the residual between hit position at TOF obtained from the time difference in two PMTs and the extrapolated track of JET to be less than 50 mm. The quality cut efficiency was estimated as 94.7±0.2 % at 0.2 GeV and 91.7±0.1 % at 2.0 GeV.

### *3.3 Particle identification*

Proton and antiproton candidates were identified with a combination of a charge selection and a mass selection as follows: (1) Particle charge, $Z$ is identified by $\mathrm{d}E/\mathrm{d}x$ measurements. We required $\mathrm{d}E/\mathrm{d}x$ measurements with both top and bottom TOF hodoscopes to be inside a band defined as a function of rigidity corresponding to singly-charged particles. (2) Particle mass $m$ is reconstructed with rigidity $R$, velocity $\beta$ and $Z$ as $m = ZeR\sqrt{1/\beta^2 - 1}$. We required $1/\beta$ to be inside a band defined as a function of rigidity as shown in Fig. 2, so that the reconstructed mass was consistent with that of a proton or antiproton. The $\mathrm{d}E/\mathrm{d}x$ and $\beta$ bands for antiprotons are defined in the same way as for protons except for the rigidity sign. The selection efficiency of each $\mathrm{d}E/\mathrm{d}x$ band cut was estimated as a fraction of the number of selected events among a proton sample selected by the other independent $\mathrm{d}E/\mathrm{d}x$ selections. The net efficiency for the two $\mathrm{d}E/\mathrm{d}x$ band cuts was 96.5±0.1 % at 0.2 GeV and 96.4±0.1 % at 2.0 GeV. The selection efficiency of the $1/\beta$ band cut was estimated as 99.5±0.2 % at 0.2 GeV and 97.0±0.1 % at 2.0 GeV.

In order to eliminate $\mathrm{e}^-$ and $\mu^-$ backgrounds that mimic relativistic antiproton candidates with $\beta > 0.9$, we applied Čerenkov veto cuts to select (3) the particle trajectory to be inside an aerogel fiducial volume, and (4) the Čerenkov outputs to be less than a threshold. The rejection factor was estimated as $(8.9\pm0.2)\times10^2$ using a relativistic proton sample with rigidity larger than 20 GV. The efficiency including a loss of fiducial volume by 18 % was estimated as 75.8±0.1 % at 0.4 GeV and 62.3±0.1 % at 2.0 GeV.

Because of the relativistic rise of $\mathrm{d}E/\mathrm{d}x$ in the JET gas, ultra-relativistic

particles ($\beta \rightarrow 1$) have $\mathrm{d}E/\mathrm{d}x$ about 1.4 times higher than minimum ionizing particles. A tight cut on $\mathrm{d}E/\mathrm{d}x$ measured with the JET can eliminate part of the $e^-$ and $\mu^-$ backgrounds. (5) We required $\mathrm{d}E/\mathrm{d}x$ measurements with the JET to be inside a band defined as a function of rigidity. The rejection factor was estimated to be 1.75±0.03 at 2.0 GeV and 4.85±0.08 at 4.0 GeV, as a fraction of the rejected events among the $e^-$ and $\mu^-$ sample. The efficiency was estimated to be 98.2±0.1 % at 2.0 GeV and 96.9±0.1 % at 4.0 GeV.

Following the particle identification procedure, 1,512 antiproton candidates were identified above 0.2 GeV as shown in Fig. 2. Antiproton candidates that have wrongly reconstructed $\beta$ and lie above the selection band were rejected by the $1/\beta$ band cuts. The antiproton flux was obtained by correcting for the cut efficiency estimated using the proton sample. The number of contaminating $e^-$ and $\mu^-$ background events within the antiproton selection band was estimated as the number of $e^-$ and $\mu^-$ events within the $1/\beta$ band divided by the total rejection factor defined above. The estimated number of background events (and the ratio to antiproton candidates) is 18.7±0.3 (8.5±0.1 %) in the 1.7–2.1 GeV band and 8.1±0.1 (4.0±0.1 %) in the 3.4–4.2 GeV band. Albedo and spillover from positive rigidity particles were negligible because of the high $\beta^{-1}$ and rigidity resolutions. To check against the "re-entrant albedo" background, we confirmed that the trajectories of all antiprotons could be traced numerically through the Earth's geomagnetic field back to the outside of the geomagnetic field [31,32].

### *3.4 Selection with top-middle TOF below 0.2 GeV*

Some of antiprotons below 0.2 GeV cannot reach the bottom TOF hodoscope due to energy and annihilation losses. To analyze such low energy events, we defined another set of selection criteria with a combination of the top and middle TOF hodoscopes. They are basically the same as those used with the top and bottom TOF, but the Čerenkov veto cuts were not applied since at low energies antiproton candidates are well separated from $e^-$ and $\mu^-$ backgrounds using only the $1/\beta$ band cut. Using the top-middle TOF selection criteria, 8 antiproton candidates were identified in the energy range 0.1–0.2 GeV.

Stopping antiprotons can generate secondaries in the upward direction that make additional tracks inside JET. Such events are rejected by the single-track selection. To recover such events, we searched for antiproton candidates among multi-track events. The major backgrounds for this search are upward moving proton secondaries generated in the lower half of the spectrometer from interactions of high energy protons. We can usually distinguish upward moving protons with $\beta$, but if the incident proton and the upward moving secondary hit the same top TOF counter, the $\beta$ is not correctly measured. We

rejected such events by applying the following cuts: (1) Stopping antiprotons cannot generate high energy secondaries because of the kinematical restriction. We required rigidities of all the tracks inside the JET to be less than 1 GV. (2) We required the distance between the two tracks at the top TOF to be larger than 150 mm. The efficiency of these cuts was estimated as 72.1±2.1 % by applying the same cuts to MC generated antiproton events. We found 31 multi-track antiproton candidates, but all of them were rejected by the cuts. According to the MC study, the total antiproton detection efficiency was increased by 11.1 % at 0.1 GeV by accepting multi-track events. This increase was treated as a systematic error, but it was smaller than the statistical error (+41%/–34%) of single-track antiproton candidates below 0.2 GeV.

### *3.5 Flux determination*

After the antiproton candidates were identified, energy-dependent corrections were applied for backgrounds and detection efficiency. Then the absolute flux at the top of the instrument (TOI) was obtained by taking account of energy loss inside the spectrometer, live time, and geometrical acceptance. The energy of each particle at TOI was calculated by summing up the ionization energy losses inside the instrument by tracing back the event trajectory. The geometrical acceptance was estimated using the simulation technique [33] to be 0.114±0.001 $m^2$sr at 0.2 GeV and 0.121±0.001 $m^2$sr at 2.0 GeV. The error arising from uncertainty in the detector alignment was estimated to be 1%.

In order to obtain the flux at the top of the atmosphere (TOA), we applied a correction for survival probability on the flux at TOI and a subtraction of the secondary component produced inside the overlying atmosphere. The survival probability was estimated as 89.1 % at 0.2 GeV and 92.4 % at 2.0 GeV based on total interaction lengths of 32.7 g/$cm^2$ at 0.2 GeV and 59.9 g/$cm^2$ at 2.0 GeV [34,35].

The atmospheric secondary antiproton flux was estimated by solving simultaneous transport equations [34,36]. At low energies below 1 GeV, there exists a significant contribution of non-annihilating inelastic interactions or so-called "tertiary" antiprotons. The interaction length used was based on Stephen's model [35], and the energy distribution of the tertiary production was tuned to reproduce the atmospheric antiproton flux measurements [37,38]. The amount of secondary subtraction was 11.8±1.7 % at 0.2 GeV and 28.6±4.1 % at 2.0 GeV. The relative error of 14.3 % is composed of uncertainty in the residual air depth (5.0%), in the cross section of primary cosmic rays with air nuclei (8.9%), and in the tertiary production (10.0%).

## 4 Results and Discussions

We obtained the antiproton flux at the TOA in the kinetic energy range 0.10–4.20 GeV as shown in Fig. 3 and tabulated in Table 1. The lowest energy was determined by the detector cutoff energy, and the highest energy was determined by the antiproton threshold energy of the aerogel Čerenkov counter. The overall uncertainties including statistical and systematic errors are –34.1%/+41.8% at 0.16 GeV and ±10.9% at 3.7 GeV with the given energy bin width. The statistical errors are dominant over the systematic errors below 1.4 GeV. Owing to the long duration observation the statistical errors were improved from the previous measurements with BESS, carried out on conventional 1 or 2 day balloon flights. Fig. 3 also shows the results from previous BESS flights from 1995 through 2002 [3,4,5,6,7], and theoretical calculations. Secondary antiproton calculations based on the standard leaky box model [9,13] modulated by a spherically symmetric modulation model [39] are shown at the modulation parameter $\phi$ =550 MV [4] during the last solar minimum period (1995+1997), and at 840 MV for BESS-Polar (2004). Calculations of the antiproton flux from evaporation of primordial black holes with an explosion rate of $0.4 \times 10^{-2}\mathrm{pc}^{-3}\mathrm{yr}^{-1}$ are shown with the same modulation parameters [12,40]. Fig. 3 also shows a calculation of secondary antiprotons with a diffusive reacceleration model with break (DRB) [10,41] modulated with a three dimensional drift model at a 30° solar magnetic field tilt angle [42,43]. The calculations with the secondary models are generally consistent with the BESS-Polar measurement. With the improved but still limited statistics, we cannot find a significant excess of antiprotons in the low energy region below 0.4 GeV.

The $\bar{\mathrm{p}}$/p ratio can provide a useful probe to study solar modulation and its charge-sign dependence. The BESS collaboration has tracked this ratio through most of a solar cycle. Fig. 4 shows the $\bar{\mathrm{p}}$/p ratio measured by BESS from 1995 through 2004 [3,4,5,6,7] in comparison with the calculations based on the drift model at various tilt angles [10,16,41]. Increasing solar activity strongly suppresses the low energy primary protons, while the secondary antiprotons are less affected because of their steeply decreasing spectrum in the low energy region. The moderate change in the $\bar{\mathrm{p}}$/p ratio during the positive solar magnetic field phase results mainly from the relatively greater suppression of primary protons, consistent with a spherically symmetric modulation model. However, as shown in Fig. 5, a rapid increase of the ratio was seen in BESS-2000, resulting from the dramatic suppression of the proton flux at solar maximum and the phase transition to the negative polarity [6]. The drift model calculations [10,16,41] are in good agreement with the time variations in the $\bar{\mathrm{p}}$/p ratio measured with BESS.

## 5 Conclusion

The first BESS-Polar experiment was carried out in Antarctica in December 2004, a transient period before the solar minimum in 2007. Using a new spectrometer with reduced material thickness and a long duration balloon flight near the Earth's south magnetic pole, the lowest energy limit of the antiproton flux was extended down to 0.1 GeV, and the statistics were improved compared with the previous BESS experiments. Model calculations of secondary antiproton spectra show good agreement with our results. The $\bar{p}/p$ ratio obtained shows that drift effects of particles in the heliospheric magnetic field are important, and that solar modulation is charge-sign dependent. For an extensive search for cosmic-ray antiprotons of primordial origin the BESS-Polar result provides an important baseline measurement of the secondary antiproton spectrum, which will be compared with a spectrum measured in December 2007 through January 2008, by the second Antarctic flight, during the solar minimum period.

## Acknowledgements

The authors thank NASA Headquarters for the continuous encouragement in this U.S.-Japan cooperative project. Sincere thanks are expressed to the NASA Balloon Programs Office at GSFC/WFF and to the NASA Columbia Scientific Balloon Facility for their experienced support. They also thank ISAS/JAXA and KEK for their continuous support and encouragement. Special thanks go to the National Science Foundation (NSF), USA, and Raytheon Polar Service Company for their professional support in the USA and in Antarctica. The authors would thank the BESS-Polar II collaborators M. Hasegawa, A. Horikoshi, K. Sakai, and N. Thakur for their contribution to the instrument performance evaluation and further cooperation. The BESS-Polar experiment is being carried out as a Japan-U.S. collaboration. It is supported by a KAKENHI(13001004) in Japan, and by NASA grants in the USA.

## References

[1] K. Yoshimura, *et al.*, Phys. Rev. Lett. 75 (1995) 3792.

[2] A. Moiseev, *et al.*, Astrophys. J. 474 (1997) 479.

[3] H. Matsunaga, *et al.*, Phys. Rev. Lett. 81 (1998) 4052.

[4] S. Orito, *et al.*, Phys. Rev. Lett. 84 (2000) 1078.

[5] T. Maeno, *et al.*, Astropart. Phys. 16 (2001) 121.

[6] Y. Asaoka, *et al.*, Phys. Rev. Lett. 88 (2002) 051101.

[7] S. Haino, *et al.*, Proc. 29th Int. Cosmic Ray Conf. (Pune) 3 (2005) 13.

[8] T. K. Gaisser and R. K. Schaffer, Astrophys. J. 394 (1992) 174.

[9] T. Mitsui, Ph.D. thesis, University of Tokyo, 1996.

[10] I .V. Moskalenko, *et al.*, Astrophys. J. 565 (2002) 280.

[11] S. W. Hawking, Commun. Math. Phys. 43 (1975) 199.

[12] K. Maki, T. Mitsui and S. Orito, Phys. Rev. Lett. 76 (1996) 3474.

[13] T. Mitsui, K. Maki and S. Orito, Phys. Lett. B 389 (1996) 169.

[14] L. Bergström, *et al.*, Astrophys. J. 526 (1999) 215.

[15] J. Clem and P. Evenson, J. Geophys. Res. 109 (2004) A07107.

[16] J. W. Bieber, *et al.*, Phys. Rev. Lett. 83 (1999) 674.

[17] A. W. Strong, I .V. Moskalenko, O. Reimer Astrophys. J. 613 (2004) 962.

[18] A. Yamamoto, *et al.*, Adv. Space Res. 30(5) (2002) 1253.

[19] J. W. Mitchell, *et al.*, Nucl. Phys. B (Proc. Suppl.) 134 (2004) 31.

[20] T. Yoshida, *et al.*, Adv. Space Res. 33(10) (2004) 1755.

[21] Y. Ajima, *et al.*, Nucl. Instrum. Methods A 443 (2000) 71.

[22] A. Yamamoto, *et al.*, IEEE Trans. Appl. Superconduct. 12(1) (2002) 438.

[23] Y. Makida, *et al.*, IEEE Trans. Appl. Superconduct. 16(2) (2006) 477.

[24] S. Haino, *et al.*, Nucl. Instrum. Methods A 518 (2004) 167.

[25] S. Haino, *et al.*, Phys. Lett. B 594 (2004) 35.

[26] M. Sasaki, *et al.*, Proc. 29th Int. Cosmic Ray Conf. (Pune) 3 (2005) 421.

[27] T. Yoshida, *et al.*, Proc. 29th Int. Cosmic Ray Conf. (Pune) 3 (2005) 33.

[28] R. Brun, *et al.*, GEANT3.21–Detector Description and Simulation Tool, CERN Program Library, Long Write up W5013.

[29] H. Fesefeldt, PITHA 85/02, Aachen, (1985).

[30] Y. Asaoka, *et al.*, Nucl. Instrum. Methods A 489 (2001) 170.

[31] M. Honda, *et al.*, Phys. Rev. D 70 (2004) 043008.

[32] International Geomagnetic Reference Field, 9th generation (2003) <http://modelweb.gsfc.nasa.gov/models/igrf.html>

[33] J. D. Sullivan, Nucl. Instrum. Methods 95 (1971) 5.

[34] S. A. Stephens Astropart. Phys. 6 (1997) 229.

[35] S. A. Stephens Proc. 29th Int. Cosmic Ray Conf. (Pune) 3 (2005) 169.

[36] P. Papini, *et al.*, Nuovo Cimento 19C (1996) 367.

[37] K. Yamato, *et al.*, Phys. Lett. B 632 (2003) 475.

[38] T. Sanuki, *et al.*, Phys. Lett. B 577 (2003) 10.

[39] L. A. Fisk, J. Geophys. Res. 76 (1971) 221.

[40] K. Yoshimura, *et al.*, Adv. Space Res. 27(4) (2001) 693.

[41] I .V. Moskalenko, Private communication, 2007.

[42] X. Zhao and J. T. Hoeksema, Adv. Space Res. 16(9) (1995) 181.

[43] The Wilcox Solar Observatory, <http://wso.stanford.edu/Tilts.html>

[44] K .Yoshimura, Adv. Space Res. in press (2007).

Table 1
Antiproton flux and $\bar{\mathrm{p}}$/p ratio at the top of atmosphere with statistical (first) and systematic (second) errors. $N_{\bar{\mathrm{p}}}$ and $N_{BG}$ are the number of observed antiprotons and estimated background events, respectively.

| Kinetic energy (GeV) | | $N_{\bar{\mathrm{p}}}$ | $N_{BG}$ | $\bar{\mathrm{p}}$ flux | $\bar{\mathrm{p}}$/p ratio |
|---|---|---|---|---|---|
| range | mean | | | $(\mathrm{m}^{-2}\mathrm{sr}^{-1}\mathrm{s}^{-1}\mathrm{GeV}^{-1})$ | |
| 0.10–0.18 | 0.16 | 8 | 0.0 | $4.37^{+1.81+0.25}_{-1.47-0.25} \times 10^{-3}$ | |
| 0.18–0.28 | 0.22 | 15 | 0.0 | $4.53^{+1.31+0.27}_{-1.11-0.27} \times 10^{-3}$ | $8.28^{+2.03+0.64}_{-2.39-0.64} \times 10^{-6}$ |
| 0.28–0.40 | 0.34 | 24 | 0.0 | $6.67^{+1.48+0.27}_{-1.30-0.27} \times 10^{-3}$ | $9.49^{+1.85+0.40}_{-2.10-0.40} \times 10^{-6}$ |
| 0.40–0.56 | 0.48 | 23 | 0.1 | $3.94^{+0.91+0.30}_{-0.80-0.30} \times 10^{-3}$ | $5.18^{+1.06+0.38}_{-1.20-0.38} \times 10^{-6}$ |
| 0.56–0.70 | 0.65 | 37 | 0.2 | $8.27^{+1.53+0.47}_{-1.39-0.47} \times 10^{-3}$ | $1.10^{+0.18+0.06}_{-0.20-0.06} \times 10^{-5}$ |
| 0.70–0.88 | 0.79 | 55 | 0.6 | $9.82^{+1.41+0.59}_{-1.29-0.59} \times 10^{-3}$ | $1.38^{+0.18+0.08}_{-0.20-0.08} \times 10^{-5}$ |
| 0.88–1.10 | 1.00 | 84 | 3.3 | $1.17^{+0.14+0.07}_{-0.13-0.07} \times 10^{-2}$ | $1.83^{+0.21+0.11}_{-0.22-0.11} \times 10^{-5}$ |
| 1.10–1.37 | 1.23 | 143 | 10.8 | $1.64^{+0.15+0.12}_{-0.14-0.12} \times 10^{-2}$ | $2.94^{+0.26+0.20}_{-0.27-0.20} \times 10^{-5}$ |
| 1.37–1.72 | 1.54 | 198 | 18.2 | $1.84^{+0.15+0.13}_{-0.14-0.13} \times 10^{-2}$ | $4.00^{+0.31+0.28}_{-0.33-0.28} \times 10^{-5}$ |
| 1.72–2.15 | 1.92 | 220 | 18.7 | $1.62^{+0.11+0.13}_{-0.11-0.13} \times 10^{-2}$ | $4.42^{+0.30+0.33}_{-0.30-0.33} \times 10^{-5}$ |
| 2.15–2.68 | 2.40 | 233 | 15.1 | $1.40^{+0.09+0.12}_{-0.09-0.12} \times 10^{-2}$ | $5.01^{+0.33+0.41}_{-0.33-0.41} \times 10^{-5}$ |
| 2.68–3.36 | 3.01 | 276 | 11.9 | $1.47^{+0.09+0.11}_{-0.09-0.11} \times 10^{-2}$ | $7.17^{+0.43+0.54}_{-0.43-0.54} \times 10^{-5}$ |
| 3.36–4.20 | 3.68 | 204 | 8.1 | $1.10^{+0.08+0.09}_{-0.08-0.09} \times 10^{-2}$ | $7.46^{+0.52+0.60}_{-0.52-0.60} \times 10^{-5}$ |

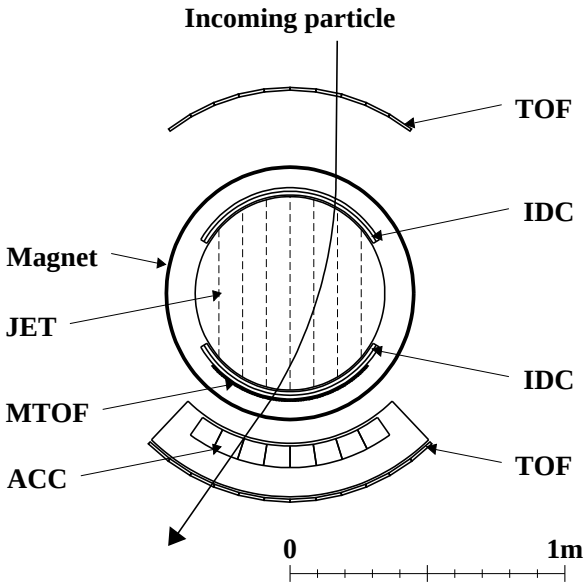


Fig. 1. Cross-sectional view of the BESS-Polar spectrometer.

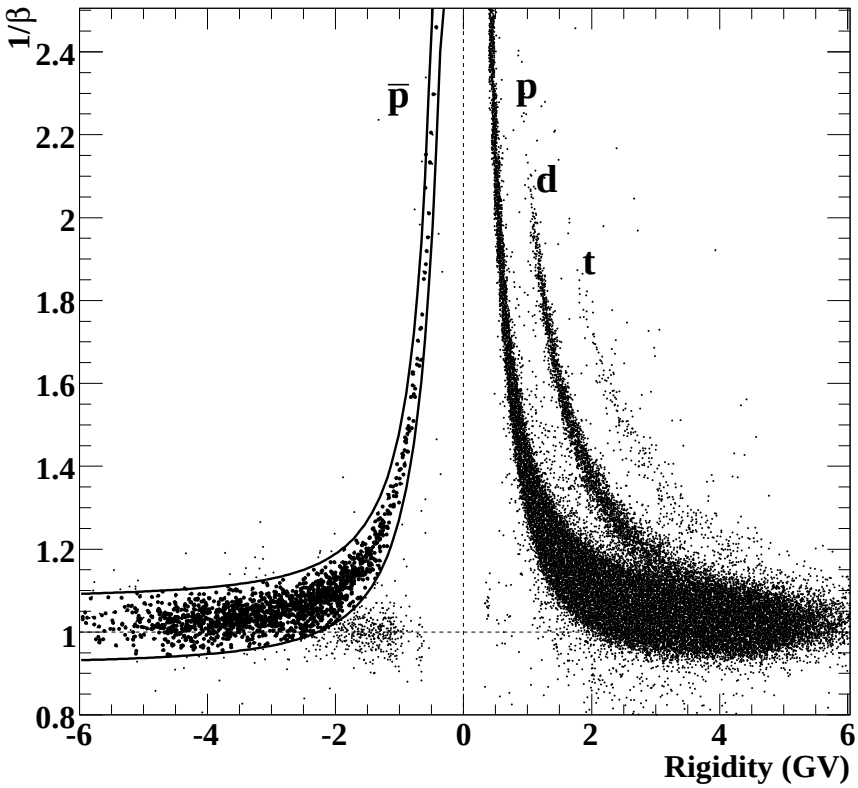


Fig. 2. The $\beta^{-1}$ versus rigidity plot, and antiproton selection band. The same band but opposite rigidity sign is applied to select protons. For the negative rigidity, all the events after Čerenkov veto cuts and JET $\mathrm{d}E/\mathrm{d}x$ cut are shown. For the positive rigidity, 0.5 % of the events after Čerenkov veto cuts are shown.

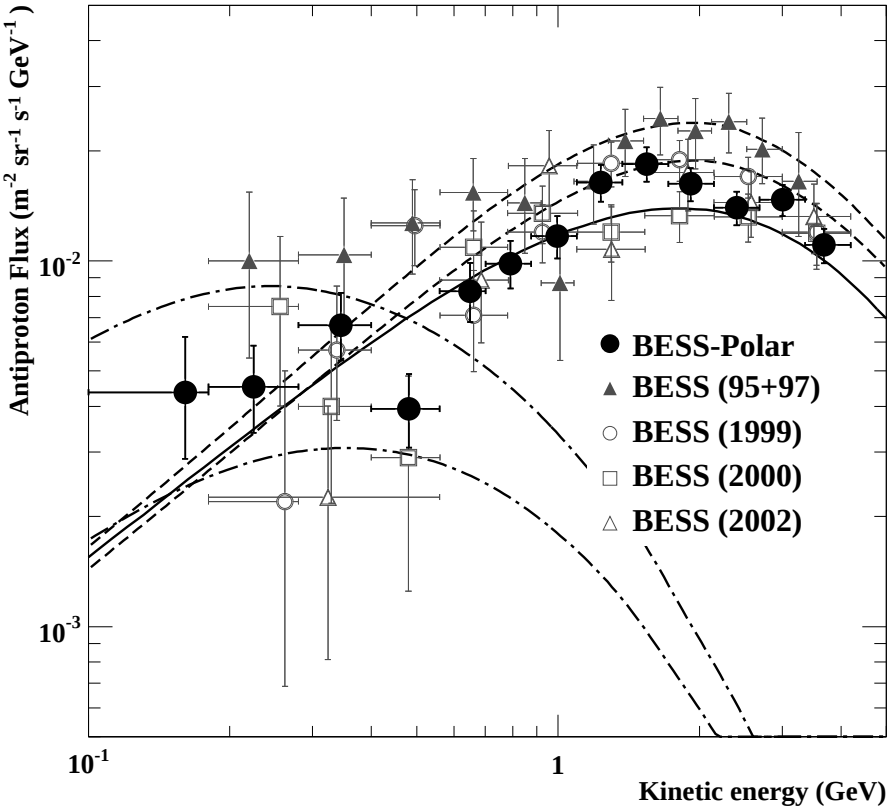


Fig. 3. Antiproton flux at the top of the atmosphere obtained with the first BESS-Polar flight together with results from previous BESS flights. The dashed curves are calculations of secondary antiproton spectra with the standard leaky box model [9,13] modulated with a spherically symmetric model [39] by 550 MV [4] (upper) and 841 MV (lower). The dash-dot curves are calculations of antiproton spectra from evaporation of primordial black holes with an explosion rate of $0.4 \times 10^{-2}\mathrm{pc}^{-3}\mathrm{yr}^{-1}$ with the same modulation parameters [12,40]. The solid curve shows a calculation of secondary antiprotons with a diffusive reacceleration model with break (DRB) [10,41] modulated with a three dimensional drift model at a 30° solar magnetic field tilt angle [42,43].

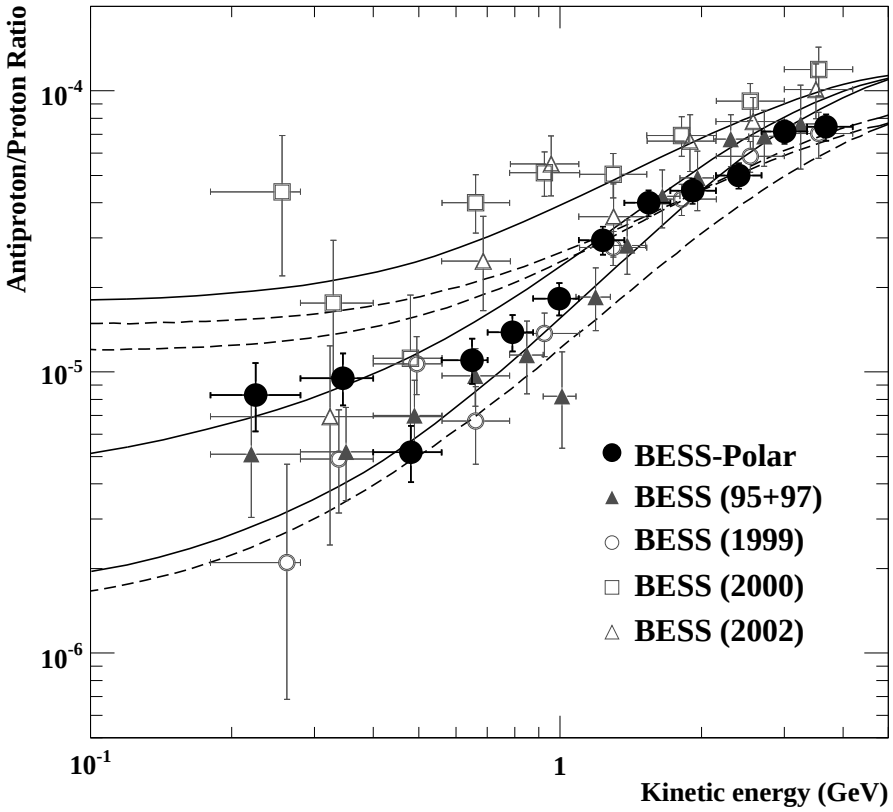


Fig. 4. $\bar{\mathrm{p}}/\mathrm{p}$ ratio obtained with the first BESS-Polar flight together with results from previous BESS flights. The dashed curves are calculations based on the drift model by Moskalenko et al. [10,41] at solar magnetic field tilt angles of (from top to bottom) $60°(A < 0)$, $30°(A < 0)$, and $10°(A > 0)$, where $A$ indicates the polarity of solar activity. The solid curves are calculations based on the drift model by Bieber et al. [16] at the same tilt angles.

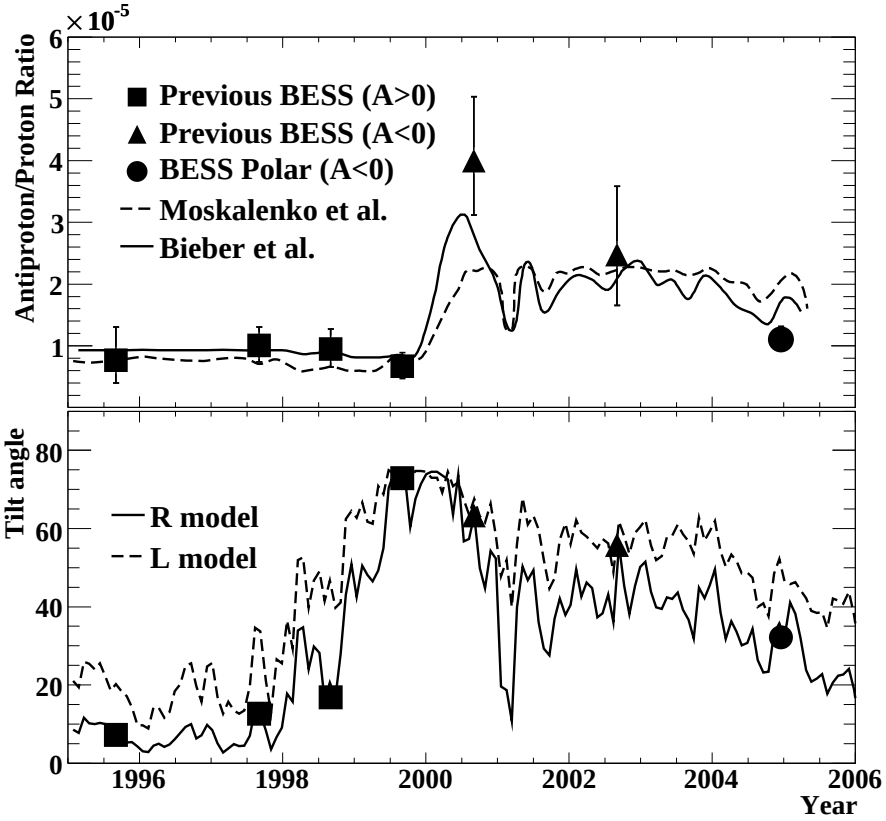


Fig. 5. Upper figure: Time variation of the $\bar{p}/p$ ratio at 0.65 GeV compared with the two drift models [10,16]. Lower figure: Time variation of heliospheric current sheet tilt angles for Hoeksema models using a radial boundary condition (R model) and line-of-sight boundary condition (L model) [42,43].